PERGAMON

International Journal of Solids and Structures 38 (2001) 5185–5203

INTERNATIONAL JOURNAL OF SOLIDS and STRUCTURES

www.elsevier.com/locate/ijsolstr

A finite element method for stress-assisted surface reaction and delayed fracture

J.H. Prevost [a,*], T.J. Baker [b], J. Liang [c], Z. Suo [c]

[a] *Civil and Environmental Engineering Department, Princeton University, Princeton, NJ 08544, USA*
[b] *Mechanical and Aerospace Department, Princeton University, Princeton, NJ 08544, USA*
[c] *Mechanical and Aerospace Department and Materials Institute, Princeton University, Princeton, NJ 08544, USA*

Received 7 April 2000

Abstract

When a stressed solid is in contact with an environment (a vapor or a liquid solution), the solid may gain mass from, or lose mass to, the environment. The surface reaction is driven by the interfacial and elastic energy and by the chemical potential difference between the solid and the environment. This paper presents a finite element method to simulate the stress-assisted surface reaction. The reduction of the total free energy associated with gaining unit volume of solid defines the driving force. A linear kinetic law is adopted, where the reaction rate is proportional to the driving force. The problem is described with a variational statement. The elastic field in the solid is solved repeatedly as the solid changes its shape. The solid shape is updated with a mesh adaptation procedure and according to the kinetic law. Numerical examples include shape changes of a wavy surface, and crack nucleation at a grain boundary.

Keywords: Finite element; Solids; Fracture; Crack; Instability; Microstructural

1. Introduction

Mullins (1959) showed that, when a wavy surface of a solid is in contact with its vapor, the surface energy causes the peaks on the solid surface to lose mass to the environment, and the valleys to gain mass. Consequently, the surface energy tends to flatten the surface. A flat solid surface is stable because any waviness will raise the total surface energy. Srolovitz (1989) examined the stability of a flat solid surface when the solid is subjected to stresses. He perturbed the surface into sinusoidal waves, and found that for surface wavelength above a critical value, evaporation and condensation processes amplify the surface waviness. Analogously, when a solid dissolves in an environment, the dissolution rate depends on stress. The stress-assisted dissolution has long been suggested as a mechanism for crack nucleation. Hillig and Charles (1965) developed a model for crack growth that accounts for the stress dependence of activation

* Corresponding author.
E-mail address: prevot@princeton.edu (J.H. Prevost).

0020-7683/01/$ - see front matter
PII: S0020-7683(00)00353-X

energy and driving force. Chuang and Fuller (1992) used the model to identify different regimes of crack tip geometry. They started with an elliptical flaw and computed the instantaneous dissolution rate on the flaw surface. Crack nucleation can also occur at a grain boundary groove of a polycrystalline material (Yu and Suo, 1999). In a corrosive environment, the groove deepens at the grain boundary and concentrates stress, which, in its turn, accelerates the surface reaction at the groove root. Such a process causes the groove root to lose equilibrium and initiate a crack.

Kim et al. (1999) developed a technique to determine the stress state on a solid surface by comparing the surface roughness, as measured by an atomic force microscope, before and after chemical etching under stress. They compared the experimental profiles to those predicted by a linear kinetic law. Aziz et al. (1991) showed that the velocity of a crystalline silicon phase growing into an amorphous silicon phase varies linearly with the applied stress. Tensile stress gives a higher growth velocity while compressive stress gives a lower velocity. This study indicates that stress state affects mobility. Furthermore, Barvosa-Carter and Aziz (1998) showed that the stress dependent mobility affects the stability of moving surface. Surface instability and crack nucleation have also been studied when surface diffusion is allowed (Chiu and Gao, 1993; Yang and Srolovitz, 1993).

A gap exists between the practical needs and the available modeling tools. The surface reaction changes the solid shape. The reaction rate depends on the stress state on the surface, as well as interfacial energy and chemical potential. As the solid surface changes shape, the stress field in the solid must be solved repeatedly. The above models rely on elasticity solutions of special geometries (e.g. ellipses, cycloids, etc.). This paper formulates a finite element method to simulate the stress-dependent surface reaction.

Mesh adaptation is accomplished in several stages. First, we calculate the motion of the mesh as dictated by surface reaction rate. Second, we coarsen the mesh to eliminate badly distorted elements. Third, we enrich the mesh to recover the mesh density. Meshing in the body close to the surface conforms to the meshing on the surface. Surface meshing is governed by the length and strain energy of the elements. The body and surface meshing are controlled by user input parameters, adjusted to insure the quality of the mesh. This work builds on our previous work (Sun et al., 1997) and the work of others (Bhate et al., 2000; Zhang and Bower, 1999; Cocks et al., 1999).

This paper assumes a linear kinetic law, which only applies when the reaction is close to equilibrium, i.e., when the driving force is small. The mobility is assumed to be stress independent. For reactions far from equilibrium, stress-dependent mobility should be considered (Yu and Suo, 2000). The main purpose of this paper is to demonstrate the numerical technique when applied to surface motion problems, rather than the exact form of the kinetic law.

2. Surface reaction model

To illustrate our computational approach, consider a specific problem described by Yu and Suo (1999). Fig. 1 illustrates the two dimensional model. A ceramic is in contact with an environment. Within the environment, the molecular mobility is so large that the chemical potential is taken to be uniform. The solid

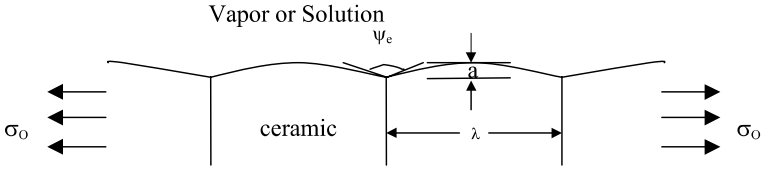

Fig. 1. A ceramic in a corrosive environment, subject to stress parallel to the surface.

and the environment, however, are not in equilibrium with each other: the solid loses mass to the environment by dissolution. The solid is subject to a stress in the horizontal direction σ_0, and remains elastic – i.e., is, no dislocation or diffusional creep occurs to alleviate the stress concentration at the groove roots. The groove depth is a, the grain size is λ, and the equilibrium dihedral angle is ψ_e. In the absence of the stress, the solid can reach a steady shape and subsequently erodes uniformly (Suo, 1997). When the stress is applied, a triple junction concentrates stress. Consequently, dissolution is faster at the groove root than elsewhere on the surface. This differential in the dissolution rate may sharpen the groove root, which then further concentrates stress. The positive feedback will lead to the nucleation of a sharp crack.

As the surface reaction proceeds, the solid environment as a system reduces its total free energy. The total free energy, G, consists of the surface energy U_S, the grain boundary energy U_B, the chemical energy U_C, the elastic energy U_E, and a term U_L due to the applied traction:

$$G = U_S + U_B + U_C + U_E - U_L \tag{1}$$

They are written explicitly as

$$G = \int \gamma_S \, dA_S + \int \gamma_B \, dA_B + \int g \, dV + \int w \, dV - \int t_i u_i \, dA_L \tag{2}$$

Here γ_S is the surface energy per unit area, γ_B is the grain boundary energy per unit area, g is the chemical potential increase per unit volume of solid added on a flat, stress-free surface, w is the elastic energy per unit volume, t_i is the applied traction, and u_i is the displacement. Traction t_i is prescribed on the surface A_L. The surface area is A_S, and the area of grain boundary is A_B.

The system is capable of three kinds of *variations*: the elastic displacement δu, the solid volume accretion per unit area δr_n, and the triple junction motion δy. The elastic energy density is a function of displacement gradient in a usual way, $w = w(u_{i,j})$. By definition g is independent of strain. We assume that γ_S and γ_B are also independent of strain. That is, we neglect the effect of surface stress. For the time being, γ_S is taken to be isotropic. Associated with the three variations, the free energy changes by

$$\delta G = \int \left(\frac{\partial w}{\partial u_{i,j}} \right) \delta u_{i,j} \, dV - \int t_i \delta u_i \, dA_L + \int (w + \gamma_S K + g) \delta r_n \, dA_S + \left(-2\gamma_S \cos \frac{\psi}{2} + \gamma_B \right) l \, \delta y \tag{3}$$

Here ψ is the dihedral angle, K is the surface curvature, and l is the length of the triple junction. We adopt the sign convention such that $K > 0$ at a peak on the solid surface.

The elastic field is taken to be in equilibrium. Consequently, the free energy variation with the displacement vanishes, namely,

$$\int \left(\frac{\partial w}{\partial u_{i,j}} \right) \delta u_{i,j} \, dV - \int t_i \delta u_i \, dA_L = 0 \tag{4}$$

This recovers the usual variational statement of equilibrium elastic field. The statement is the basis for the finite element method to determine the elastic field in a solid once the surface shape and the traction are given. The solid and the environment are not in equilibrium with each other. Consequently, the free energy variation associated with unit volume of solid grown on the surface does not vanish; rather, it defines a driving force:

$$p = -w - \gamma_S K - g \tag{5}$$

When $p = 0$, the solid is in equilibrium with the environment. When $p > 0$, the solid gains mass from the environment. When $p < 0$, the solid loses mass to the environment. Similarly, the free energy variation with the triple junction motion defines a driving force on the junction:

$$f = 2\gamma_S \cos \frac{\psi}{2} - \gamma_B \tag{6}$$

The actual normal velocity of the surface, v_n, is a function of the driving force. For simplicity, we adopt a linear kinetic law:

$$v_n = mp \tag{7}$$

Here m is the specific reaction rate and is regarded as an input of the simulation. Because surface reaction is a thermally activated process, m depends on temperature in the usual way, $m = m_0 \exp(-q/kT)$, where m_0 is the frequency factor, q is the activation energy, k is the Boltzmann's constant, and T is the temperature. The linear kinetic law (7) is a special case of a more general law introduced by Hillig and Charles (1965) and is valid when the driving force is small compared to the average thermal energy. Nonlinear kinetic laws will be discussed in a separate communication. Furthermore, we adopt a linear kinetic law for the triple junction:

$$\dot{y} = m_t f \tag{8}$$

where $\dot{y}$ is the velocity of the triple junction, and m_t is the junction mobility.

Eq. (4) defines the regular elasticity problem. At a given time, the solid shape is known, and the stress field is determined by solving a boundary value problem. Eqs. (5) and (7) determine the surface reaction rate, v_n, which, once determined, updates the surface shape for a time step. The whole procedure repeats for the next time step. Eq. (6) defines the driving force for the triple junction, f. The triple junction will be assumed to be in equilibrium at all times so that $f = 0$. In numerical implementation, we need not enforce $f = 0$. Rather, we set a large value of junction mobility m_t. This approach follows that in Sun et al. (1997).

Following a procedure described by Suo (1997), we now formulate a variational statement for surface reaction. Recall that p is the free energy reduction associated with a unit volume of mass attached coherently to the solid surface. When a surface element dA_S moves by a distance δr_n, the free energy reduces by $p\delta r_n dA_S$. In addition, there is an independent motion of the triple junction by δy. Let f be the driving force on the triple junction of length l. Consequently, associated with the entire surface motion, the total free energy variation, δG, is given by

$$fl\delta y + \int p\delta r_n \, dA_S = -\delta G \tag{9}$$

The integral is over the surface. Because δr_n is an arbitrary virtual motion, this relation defines the driving force for the surface reaction p, at every point on the surface. Similarly, since δy is also an arbitrary virtual motion, f is the free energy reduction of the system per unit length and motion of the triple junction. Note that in Eq. (9) we have assumed that the elastic displacement field is in equilibrium so that the free energy variation with displacement field vanishes. Thus Eq. (9) is identical to Eq. (3) once we identify p and f by Eqs. (5) and (6).

Eliminating p and f from Eqs. (7)–(9), we obtain that

$$\frac{\dot{y}}{m_t} l\delta y + \int \frac{v_n}{m} \delta r_n \, dA_S = -\delta G \tag{10}$$

This is the variational statement for the surface reaction.

3. Discretization of surface

The system consists of two coupled subsystems: the solid surface and the solid body. The surface motion is affected by the strain energy within the solid body, which in turn is affected by the shape changes due to the surface motion. Each subsystem is discretized into finite elements as follows.

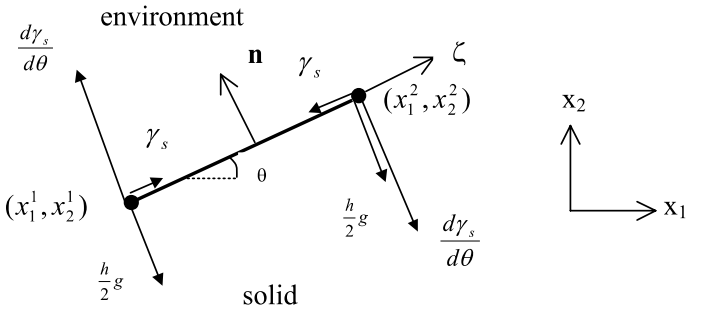

Fig. 2. A surface element along with the nodal forces exerted on the element.

Following Sun et al. (1997), represent the surface by a set of linear isoparametric finite elements. Fig. 2 illustrates a representative element. The element is defined by two nodes, (x_1^1, x_2^1) and (x_1^2, x_2^2). Let h be the element length and θ be the element slope. They relate to the coordinates of the two nodes as

$$x_1^2 - x_1^1 = h\cos\theta, \qquad x_2^2 - x_2^1 = h\sin\theta \tag{11}$$

The unit normal to the element is $\mathbf{n} = [-\sin\theta, \cos\theta]$. A point on the line element is given by

$$\mathbf{x} = \sum_{a=1}^{2} N^a \mathbf{x}^a \tag{12}$$

where N^a are the usual linear shape functions, viz.

$$N^a = \frac{1}{2}(1 + \zeta^a\zeta) \quad -1 \leqslant \zeta \leqslant +1 \tag{13}$$

where ζ is a local coordinate, and ζ^a are the local coordinates of nodes 1 and 2 $\left(\zeta^1 = -1; \zeta^2 = +1\right)$. Let $\mathbf{v}^1$ and $\mathbf{v}^2$ be the velocities of the two nodes. The velocity of a point on the surface is

$$\mathbf{v} = \dot{\mathbf{x}} = \sum_{a=1}^{2} N^a \mathbf{v}^a = \sum_{a,i} N^a v_i^a \tag{14}$$

The normal velocity is

$$\mathbf{v}_\mathrm{n} = \mathbf{v}\cdot\mathbf{n} = \sum_{a,i} N^a v_i^a n_i \tag{15}$$

For this one element, the left-hand side of Eq. (10) becomes

$$\delta x_i^a H_{ij}^{ab} v_j^b \tag{16}$$

with

$$H_{ij}^{ab} = \int_{-1}^{+1} \frac{1}{m} N^a n_i N^b n_j \frac{h}{2}\mathrm{d}\zeta \tag{17}$$

Upon integration, Eq. (17), gives

$$H_{ij}^{ab} = \frac{h}{6m}\begin{bmatrix} 2\sin^2\theta & -2\sin\theta\cos\theta & \sin^2\theta & -\sin\theta\cos\theta \\ -2\sin\theta\cos\theta & 2\cos^2\theta & -\sin\theta\cos\theta & \cos^2\theta \\ \sin^2\theta & -\sin\theta\cos\theta & 2\sin^2\theta & -2\sin\theta\cos\theta \\ -\sin\theta\cos\theta & \cos^2\theta & -2\sin\theta\cos\theta & 2\cos^2\theta \end{bmatrix} \tag{18}$$

The free energy variation associated with a given element is computed as follows:

$$\delta G = \gamma_S \delta h + \frac{\partial \gamma_S}{\partial \theta} h\,\delta\theta + \int (w+g)\,\delta x_n\,\mathrm{d}A_S \tag{19}$$

Here we have allowed anisotropic surface energy. That is, γ_S, is a function of θ. The anisotropy, $\partial\gamma_S/\partial\theta$, gives rise to a moment on the element, as indicated in Fig. 2. Eq. (19) leads to the following set of nodal forces f_i^a, viz.,

$$\delta G = -f_i^a\,\delta x_i^a \tag{20}$$

where

$$f_i^a = \gamma_S\begin{bmatrix} \cos\theta \\ \sin\theta \\ -\cos\theta \\ -\sin\theta \end{bmatrix} + \frac{\partial\gamma_S}{\partial\theta}\begin{bmatrix} -\sin\theta \\ \cos\theta \\ \sin\theta \\ -\cos\theta \end{bmatrix} + \frac{h}{2}\begin{bmatrix} ((2/3)w^1 + (1/3)w^2)\sin\theta \\ -((2/3)w^1 + (1/3)w^2)\cos\theta \\ ((1/3)w^1 + (2/3)w^2)\sin\theta \\ -((1/3)w^1 + (2/3)w^2)\cos\theta \end{bmatrix} + \frac{h}{2}g\begin{bmatrix} \sin\theta \\ -\cos\theta \\ \sin\theta \\ -\cos\theta \end{bmatrix} \tag{21}$$

Here w^1 and w^2 are the nodal values of the strain energy density function, and we interpolate w linearly along the element.

Assemble the coordinates of all nodes into a column $\mathbf{x}$, and the forces on all nodes into $\mathbf{f}$, and the virtual motion of all nodes into $\delta\mathbf{x}$. Eq. (10) then becomes

$$(\delta\mathbf{x})\cdot\left(\mathbf{H}\dot{\mathbf{x}}\right) = (\delta\mathbf{x})\cdot\mathbf{f} \tag{22}$$

Since the equations are to hold for any variation $\delta\mathbf{x}$, we obtain that

$$\mathbf{H}\dot{\mathbf{x}} = \mathbf{f} \tag{23}$$

The matrix $\mathbf{H}$ relates the surface velocity to the applied surface and body forces. It is a symmetric matrix, and is usually positive definite. However, if part of the surface becomes flat, $\mathbf{H}$ becomes singular since a node on a flat surface may move either normal to the surface, or along the surface. The latter motion does not change the surface shape and has no physical significance. To circumvent the difficulty, we add small positive numbers to the diagonal elements of $\mathbf{H}$ to prevent it from becoming singular. These small numbers physically corresponds to additional viscosities of the nodes (Sun et al., 1997). Their exact values are unimportant, but should be large enough to stabilize the matrix, and small enough not to affect noticeably the solution accuracy. In practice, we have found that values of the order 10^{-3}–$10^{-6}\,L/m$ are adequate, where m is the surface mobility and L is a representative length of the system under study, such as the grain size.

Since $\mathbf{H}$ depends on the current position, Eq. (23) is a set of non linear ordinary differential equations. They are integrated by using an explicit fifth-order Runge–Kutta scheme (Cash and Karp, 1990), with adaptive step-size control to monitor accuracy.

4. Discretization of solid body

The strain energy density on the surface affects the surface motion. Although we can use the boundary element method to determine the elastic energy on the surface, we choose to discretize the solid body and

use the finite element method. The resulting code can then be easily extended to include effects like plasticity and creep.

The elasticity equation (4) is solved by using the standard finite element procedure. (Hughes, 1987; Zienkiewicz and Taylor, 1991). We use a finite element code, Dynaflow, developed at Princeton University over the last 20 years. The mesh is constrained to conform to the surface geometry. Mesh refinements near the crack tip are required to resolve the near singularity in the nearby stress field. An h- and r-adaptive scheme is used to conform the finite element mesh to the evolving geometry of the surface and crack tip. This is further discussed below.

Once the displacement field is solved, the elastic energy density is evaluated from the given function $w(u_{i,j})$. The resulting strain energy density field is discontinuous from element to element, and is computed with the most accuracy at the center of each finite element (Barlow, 1976). To project the resulting field onto the surface nodes, we use a least-squares procedure. Let w^h denote the elemental discontinuous strain energy density field, and $\tilde{w}$ the smoothed nodal field, viz.,

$$\tilde{w} = \sum_A N^A \tilde{w}^A \tag{24}$$

where the summation extends over all the nodes of the finite element mesh. The interpolation functions N^A are taken to be the same as the ones used to interpolate the displacement field in the elasticity problem. The least-squares procedure defines $\tilde{w}$ by minimizing

$$\int_\Omega \left(\tilde{w} - w^h\right)^2 \mathrm{d}\Omega \tag{25}$$

with respect to the $\tilde{w}^A$'s and gives rise to the following matrix problem:

$$\mathbf{Y}\tilde{\mathbf{w}} = \mathbf{w} \tag{26}$$

where the construction of the matrix $\mathbf{Y}$ and vector $\mathbf{w}$ are performed in the usual element-by-element fashion, viz.,

$$\left[\mathbf{Y}^{ab}\right]^{\mathrm{e}} = \int_{\Omega^{\mathrm{e}}} N^a N^b \mathrm{d}\Omega \tag{27}$$

$$[w^a]^{\mathrm{e}} = w^{\mathrm{e}} \int_{\Omega^{\mathrm{e}}} N^a \mathrm{d}\Omega \tag{28}$$

The matrix $\mathbf{Y}$ is symmetric, positive definite and possesses a band-profile structure. Additional simplifications are engendered by replacing $\mathbf{Y}$ by an associated diagonal matrix. It is also well established (Lee et al., 1979) that higher accuracy is achieved when $\mathbf{Y}$ is diagonal. Thus, we use nodal quadrature to diagonalize $\mathbf{Y}$ and approximate $\mathbf{Y}$ by the following matrix:

$$\left[\mathbf{Y}^{ab}\right]^{\mathrm{e}} = \delta^{ab} j^{\mathrm{e}}(\zeta^a) \tag{29}$$

where j^{e} is the jacobian determinant evaluated at node a. Consistent with this approximation, we compute the integral in Eq. (27) as:

$$[w^a]^{\mathrm{e}} = w^{\mathrm{e}} j^{\mathrm{e}}(\zeta^a) \tag{30}$$

5. Mesh adaptation

We need to adapt for two reasons. First, surface reaction changes the shape of the solid, so that the mesh of the solid must adapt to conform at each time step with the moving surface. Second, the strain energy is

highly nonuniform, so that small elements must be placed in locations where the strain energy is large. We refer to the former as dynamic adaptation and to the latter as static adaptation. The algorithm for static adaptation is a subset of that used for dynamic adaptation. We shall therefore describe dynamic adaptation in some detail and then briefly show how this technique can be applied to static adaptation. A high quality mesh with good grading in element size should be created at each time step, and the mesh adaptation algorithm should be designed to attain this goal.

Let B be the position of the material surface at a given time. During time step Δt the boundary B of the solid body is displaced to a new position B' corresponding to the updated position of the material surface. We wish to create a new mesh at time step $(t + \Delta t)$ that conforms to the boundary B' and maintains a mesh quality comparable to that of the mesh at time t.

The first operation consists of a mesh movement or r-refinement to create a valid mesh conforming to boundary B' whose elements all retain a positive area although the mesh quality may have been severely degraded. The second operation uses a mesh coarsening technique to remove mesh points and thus eliminate elements that are highly deformed. The final operation consists of a mesh enrichment scheme to recover a mesh whose point density is compatible with the boundary point distribution on B' and such that all elements are of high quality.

5.1. Mesh motion (r-adaptivity)

The finite element mesh on the solid body must adapt to the moving surface boundary. For example, the mesh is locally refined close to the crack tip and has a higher resolution close to the moving surface boundary than in the far field. Under these circumstances, classical methods (such as moving the mesh proportional to the primary boundary motion) break down, resulting in overlapping of the elements. To prevent the inversion of small elements and to accommodate high gradients in the meshing, we compute the mesh motion $\mathbf{U}$ by solving the following modified Laplace equation:

$$\nabla \cdot [(1 + \tau)\nabla \mathbf{U}] = 0 \quad \text{in the body} \tag{31}$$

with $\mathbf{U}$ restricted to conform to the surface motion, viz.,

$$\mathbf{U} = \overline{\mathbf{U}} \quad \text{on the surface} \tag{32}$$

where $\overline{\mathbf{U}}$ is the known motion of the surface. In Eq. (30), τ is a bounded, nondimensional function that is designed to prevent the inversion of small elements (Masud and Hughes, 1993) as

$$\tau^{\mathrm{e}} = \frac{\Delta_{\max} - \Delta_{\min}}{\Delta^{\mathrm{e}}} \tag{33}$$

where Δ^{e} is the area of the current element, $\Delta_{\max}$ and $\Delta_{\min}$ the maximum and minimum areas of all the elements in the mesh, respectively. Note that for the degenerate case $\Delta_{\max} = \Delta_{\min} = \Delta^{\mathrm{e}}$, $\tau = 0$ and Laplace equation works well, without the additional constraint over the elements.

5.2. Mesh coarsening

Mesh coarsening is based on an edge collapse procedure. We use three noded triangular elements in this case. Given a triangle that is a candidate for removal we take its shortest edge and allow the two endpoints of this edge to collapse to a single point. If the triangle is interior to the solid body (i.e. none of the vertices is on the boundary) the two endpoints are collapsed to the midpoint of the edge. If the triangle is not interior (i.e. at least one vertex lies on the boundary) then two possibilities arise. If the shortest edge lies in the boundary then no action is taken. If one vertex of the shortest edge lies on the boundary and the other vertex is interior then the edge is collapsed to the boundary point. As a result, this edge together with the

two incident triangles is removed from the triangulation, and the number of points in the mesh decreases by one. The effect of this operation, when repeatedly applied to a region of the triangulation, will result in a much coarser distribution of points. Unfortunately, the quality of the triangulation is also severely degraded. The mesh enrichment algorithm described in Section 5.3 dramatically improves the mesh quality, but even better results are obtained if the coarsened mesh is optimized prior to mesh enrichment. The coarsened mesh is optimized by swapping diagonals in order to maximize the minimum of the six angles of any pair of triangles with a common edge which form a convex quadrilateral. This operation will lead to the Delaunay triangulation of the coarsened point set for any planar triangulation (Lawson, 1977).

To implement the mesh coarsening procedure we need to identify those elements that have become badly distorted during the mesh movement stage. An effective element quality measure is the ratio L/r, where L is the average edge length and r is the in-radius. In terms of the three edge lengths s_1, s_2, and s_3 we find that

$$L = \frac{1}{3}(s_1 + s_2 + s_3) \tag{34}$$

$$2\Delta = r(s_1 + s_2 + s_3) \tag{35}$$

where Δ is the triangle area. It follows that

$$\frac{L}{r} = \frac{(s_1 + s_2 + s_3)^2}{6\Delta} \tag{36}$$

Alternatively, if α and β are any two angles of the triangle, it can be shown that

$$\frac{L}{r} = \frac{(\sin\alpha + \sin\beta + \sin(\alpha + \beta))^2}{3\sin\alpha\sin\beta\sin(\alpha + \beta)} \tag{37}$$

The minimum value of L/r is $2\sqrt{3}$ which is attained by an equilateral triangle. Triangles with a minimum angle near zero or a maximum angle close to 180° will exhibit large values of L/r.

5.3. Mesh enrichment

Our approach to mesh enrichment uses a Delaunay algorithm combined with a point placement strategy that creates a triangulation with provably good properties. We first compute a length density function ρ that determines the linear size of each cell. Values of this density function are defined at each boundary point as the average edge length of the two incident boundary edges. Values of the density function at all interior points of the solid body can be determined by solving the Laplace equation on the existing mesh with the predefined values of the density function at the mesh boundary being used as a Dirichlet boundary condition. It follows that the distribution of the density function inside the solid body varies smoothly and reflects the variation of the point density on the boundary.

In contrast to the Laplace solver exploited by the mesh movement procedure, a numerically less accurate but computationally faster algorithm can be used to determine the point density function throughout the solid body. Suppose that there are k edges incident to the point r_0 and let r_i, $i = 1, \ldots, n$ be the endpoint, opposite to r_0, of the ith edge. We approximate the Laplace equation

$$\nabla^2\rho = 0 \tag{38}$$

by accumulating the edge differences. Thus,

$$\sum_{i=1}^{k}(\rho_i - \rho_0) = 0 \tag{39}$$

Let ρ_i^n be the value of ρ_i after n iterations. A simple point relaxation scheme is obtained by setting

$$\rho_0^* = \frac{1}{k}\sum_{i=1}^{k}\rho_i^n \tag{40}$$

$$\rho_0^{n+1} = \omega\rho_0^* + (1-\omega)\rho_0^n \tag{41}$$

where $0 < \omega < 1$.

After establishing the length density function at all mesh points it is possible to compare the size, or more specifically the circum-radius, of each element with the average of the density function values at the element vertices. The element is marked for refinement if the circum-radius is too large when compared with the length density function. If a triangle is selected for refinement, a new mesh point is introduced at its circumcenter. The new point is inserted into the mesh by a local mesh reconstruction procedure that exploits a constrained Delaunay algorithm.

The algorithm can be applied to any valid mesh irrespective of whether the original mesh was itself Delaunay. Specifically, the triangles to be removed are those whose circumcircles contain the new point subject to the constraint that no boundary edge should be removed and that the new point is always visible from the exposed edges of the remaining triangles. It turns out that if the original triangulation is close to Delaunay then placing new points at the circumcenters of the existing triangles will create a mesh with a bound of 2 on the ratio of maximum to minimum edge length and a bound of 1 on the ratio of circum-radius to minimum edge length for all interior triangles (Baker, 1994). These bounds are sufficient to guarantee that the minimum angle is bounded below by 30° for planar triangulations (Baker, 1994, Chew, 1993). If, as proposed above, the mesh is smoothed after coarsening then the resulting mesh will be Delaunay and the above guarantee of mesh quality will always be valid. The theoretical guarantees of mesh quality do not hold for elements adjacent to the boundary but, in almost all cases, the procedure creates meshes with good quality elements near the boundary.

5.4. Static adaptation

Enrichment of the mesh in regions of high strain energy is achieved by a modification of the refinement procedure described above. Let w be the strain energy density, $\langle w\rangle$ the average value and σ the standard deviation. We form the following adaptation sensor,

$$\eta = \max\left(0, \frac{w - \langle w\rangle - \theta\sigma}{\sigma}\right) \tag{42}$$

where θ is a user defined constant. Thus η is a nonnegative function that is positive when w exceeds θ standard deviations above its average value. We replace the length density function ρ by the modified form

$$\tilde{\rho} = \frac{\rho}{1+\alpha\eta} = \begin{cases} \rho & \text{if } w \leqslant \langle w\rangle + \theta\sigma \\ \frac{\rho}{1-\alpha\theta+\frac{\alpha}{\sigma}(w-\langle w\rangle)} & \text{otherwise} \end{cases} \tag{43}$$

where α is a second user defined constant. Thus α controls the degree of local refinement while θ controls the extent of the solid body over which refinement is applied.

6. Global algorithm

The implementation and synchronization of the equations are achieved by defining solution staggers as follows:

- solid stagger: solves elasticity problem
- surface stagger: computes surface motion
- mesh stagger: computes solid mesh motion to conform to surface mesh motion

A step-by-step integration of the equations is performed, and for each time step dt, the calculations proceed as follows:

1. Solve elasticity problem on current configuration:
   - compute strain energy density
   - project onto surface nodes.
2. compute new surface configuration,
3. compute mesh motion,
4. adaptively modify mesh (r- and h-adaptivity),
5. Update time.

7. Examples

Several examples are given here to illustrate the versatility and accuracy of the numerical procedure. In all examples, we set $g = 0$. That is, a flat, unstressed solid is in equilibrium with the environment. In the examples, the solid is subjected to a uniform stress field σ_0 in the far field. Under the assumption of small perturbations, Srolovitz (1989) obtained an analytical solution:

$$y(x,t) = \frac{-m\sigma_0^2 t}{2E} + A\exp\left[-m\left(\gamma_S k^2 - \frac{2\sigma_0^2}{E}k\right)t\right]\cos(kx) \tag{44}$$

where y is the position of the surface, A is the initial amplitude of the cosine surface, $k = 2\pi/\lambda$, λ is the wavelength, and E is the Young modulus. Eq. (44) includes the result of surface energy due to Mullins (1959). We have also added the first term that corresponds to the uniform mass loss caused by elastic energy. In our numerical examples, $\lambda = 10$.

A dimensionless parameter characterizing the relative significance of the elastic and surface energy is

$$s = \frac{\sigma_0^2\lambda}{E\gamma_S} \tag{45}$$

We define a normalized time:

$$\tau = tm\gamma_S(2\pi/\lambda)^2 \tag{46}$$

7.1. Uniform surface motion

In this case, $A = 0$, i.e., the solid surface is perfectly flat. The stress raises the energy of atoms in the solid relative to that in the environment. Consequently, the solid loses mass to the environment, and the surface moves downward uniformly, according to the first term in Eq. (43). A simple uniform finite element mesh is used as shown schematically in Fig. 3 with $h/\lambda = 0.05$. Four-node bilinear finite elements are used to discretize the solid with $\Delta x/\lambda = \Delta y/\lambda = 0.05$. $s = 10$ is used. The finite element solution for this problem (not shown) is exact up to the accuracy of the Runge–Kutta scheme.

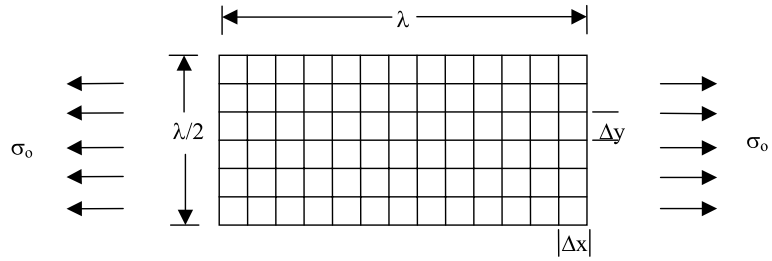

Fig. 3. Schematic mesh with labeled dimensions. For Section 7.2, the surface would be a small amplitude cosine curve. For Section 7.2.2, the mesh would be graded vertically, more refined near the surface.

7.2. Undulating surface

In this case $A \neq 0$. To assess the accuracy of the numerical procedure, a measure of error is defined as:

$$\text{error} = \frac{\int_0^{\lambda} |y - \bar{y}| \mathrm{d}x}{\int_0^{\lambda} y \, \mathrm{d}x} \tag{47}$$

where $\bar{y}$ is the numerical solution. Two cases are considered as follows.

7.2.1. Stress-free solid

In this case, $s = 0$ and the surface energy acts alone. The surface changes shape to reduce its curvature. Over time, the wavy surface will become flat. Fig. 4 shows the surface profile for various times. The data point labels indicate the numerical solution while the continuous solid line represents the analytical solution. The initial amplitude A of the surface cosine undulation is taken as $A/\lambda = 0.001$, and the solid body is discretized with four-node bilinear elements with $\Delta x/\lambda = 0.02$ and $\Delta y/\lambda = 0.05$. To compare to the analytical solution given by Mullins (1959), we limited calculation to $Ak \ll 1$, where A is the current surface amplitude. The computed error (47) is always less than 0.03%.

7.2.2. Stressed solid

When the stress σ_0 is applied, the wavy surface can either increase or decrease in amplitude depending on k. For our case, λ has been selected such that there is always a growth in amplitude (44). Two initial amplitudes were used, $A/\lambda = 0.001$ and 0.005, respectively. The mesh beneath the surface was curved ac-

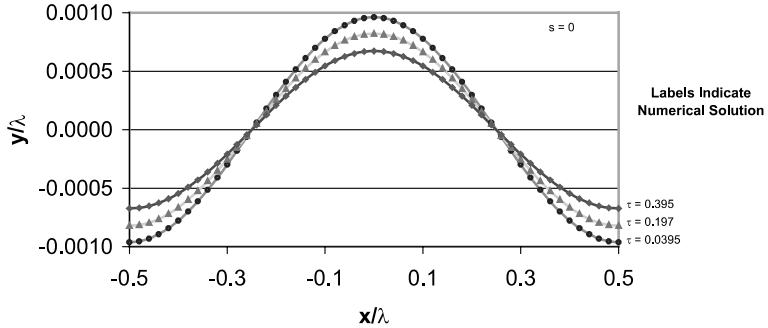

Fig. 4. Undulating surface with no applied stress: $A/\lambda = 0.001$, $h/\lambda = 0.02$, $\Delta x/\lambda = 0.02$, $\Delta y/\lambda = 0.05$.

cording to the surface and vertically graded, with a higher density near the surface and a gradually lower density moving away from the surface. The $\Delta y/\lambda$ of the first layer of elements from the surface was 0.0005. The surface was divided into 10, 100, and 1000 elements so that $\Delta x/\lambda$ would be 0.1, 0.01 and 0.001, respectively. The total number of time steps was increased from 10 to 100 to 1000 to examine numerical convergence. Representative graphs of the surface shape for each A at various times are given in Figs. 5 and 6. The errors are presented in Figs. 7 and 8. It is only possible to see the difference between the analytical and numerical solution in Fig. 6 for $\tau = 0.395$; for the other plots in Figs. 5 and 6, the analytical and numerical solutions lay right on top of each other. From Fig. 7, it is apparent that the errors become insensitive to the number of surface elements after more than 100 surface elements are used. In addition, from Fig. 8, the errors also become insensitive to the total number of time steps used after more than 100 total time steps are used. Calculations done with the finest mesh and the largest total number of time steps give the smallest error, and the error is smaller for the smaller initial amplitude problem than for the larger initial amplitude problem.

When comparing errors at shorter times, the persistence of the errors can be attributed to the finite depth of the mesh used. In the derivation of the analytical solution, the solid is assumed to be semi-infinite in depth. For longer times, the errors stop to decrease due to several reasons. As before, the finite depth of the mesh is one source of error. In addition, the surface amplitude gets larger which makes the analytical

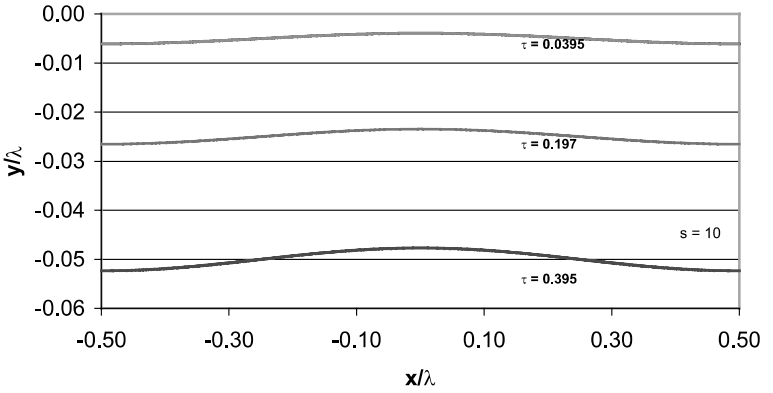

Fig. 5. Undulating surface with applied stress: $A/\lambda = 0.001$, $h/\lambda = 0.001$, $\Delta x/\lambda = 0.001$, $\Delta y/\lambda = 0.0005$, $\Delta\tau = 0.000395$.

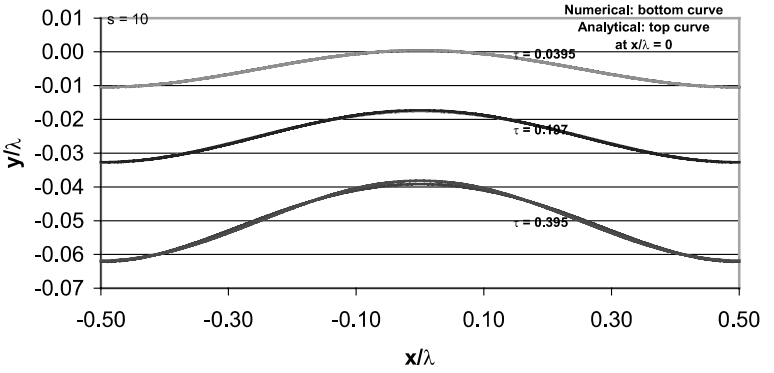

Fig. 6. Undulating surface with applied stress: $A/\lambda = 0.005$, $h/\lambda = 0.001$, $\Delta x/\lambda = 0.001$, $\Delta y/\lambda = 0.0005$, $\Delta\tau = 0.000395$.

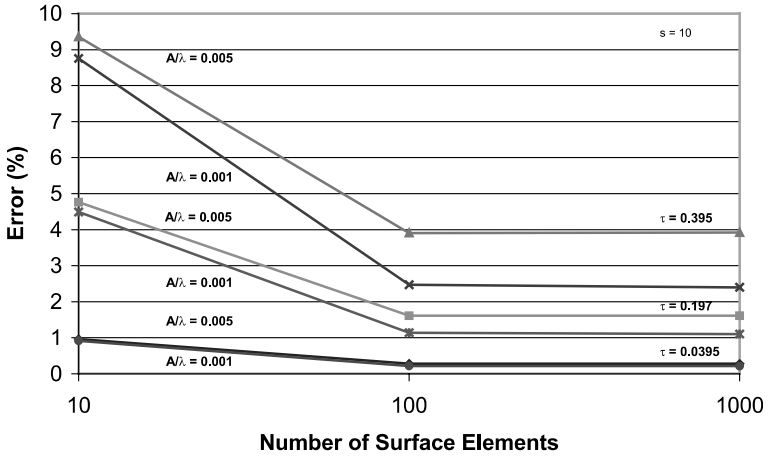

Fig. 7. Undulating surface with applied stress – error vs. number of surface elements: $\Delta\tau = 0.000395$, $\Delta x/\lambda = 0.001$, $\Delta y/\lambda = 0.0005$.

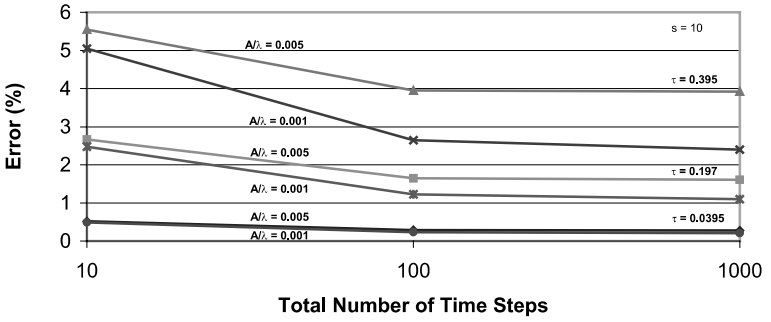

Fig. 8. Undulating surface with applied stress – error vs. total number of time steps: $h/\lambda = 0.001$, $\Delta x/\lambda = 0.001$, $\Delta y/\lambda = 0.0005$.

solution less reliable. Even if the numerical solution, which does not make the small amplitude assumption, should get more accurate, the comparison to a less accurate analytical solution would cause the error to persist.

7.3. Crack nucleation at a grain boundary

We now return to the problem depicted in Fig. 1. Yu and Suo (1999) solved the elastic stress field in a solid body analytically by using a conformal mapping method and used the variational technique to update the surface shape. The initial surface was taken to be flat. At small stresses, the surface approaches a steady shape, the solid loses mass evenly over the entire surface, and no crack is formed. At large stresses, the shape change is localized, and a crack nucleates. Several dimensionless parameters are used to measure the relative magnitude of the energetic forces in addition to s. They are

$$\Gamma = \frac{\gamma_B}{\gamma_S}, \qquad \chi = \frac{g\lambda}{\gamma_S} \tag{48}$$

For this example, the parameters are set as $\lambda = 10$, $\Gamma = 0.5$, and $\chi = 0$. The initial solid is meshed by the Delaunay method using three-node triangular elements (Fig. 9a). As the surface shape evolves, the meshing

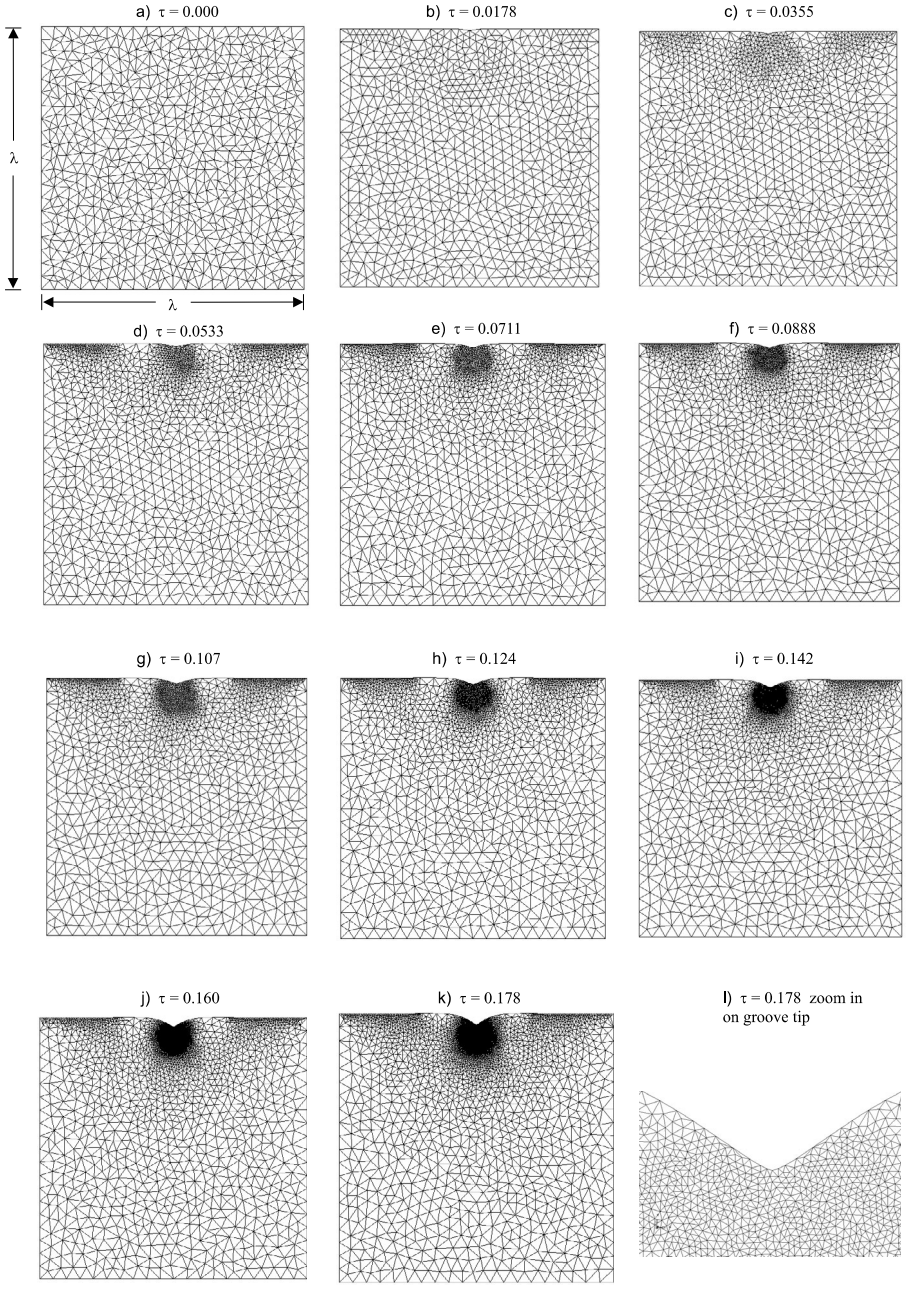

Fig. 9. Mesh development for $s = 10$.

near the groove tip is increased according to the technique described in the numerical implementation section. A representative example of the development of the meshing at the groove is shown in Fig. 9, which shows the temporal adaptation of the meshing as the crack nucleates for the case $s = 10$. At $\tau = 0$, $h/\lambda = 0.05$ whereas at the final stage $h_{\min}/\lambda = 70$, and the mesh density near the crack tip has increased by over three orders of magnitude.

Nucleation of a crack is detected when a jacobian error is detected. This means that at least one element has been inverted. Inversion of elements is due to the fact that the surface nodes are moving faster than the nodes underneath; as a result, the surface actually moves into the solid causing the program to end. Care must be taken to make sure that the computation ends not only because the elements at the groove tip inverts but that there is also a progressive increase in the growth rate of the groove depth. In addition, one should also check the strain energy to make sure that the ratio of maximum to minimum strain energy is reasonably high to result in nucleation. Another parameter that is useful to monitor is the number of Runge–Kutta integration steps that have been performed. Normally, as the conditions at the groove tip gets more unstable, more and more Runge–Kutta integration steps need to be performed.

A procedure was adopted for the computation of this example. Each case was run first with a crude time step with remeshing at every time step. This initial trial run yielded an approximate time at which crack nucleation initiates, and almost always the meshing at the groove tip was poor. Then the computation is done with remeshing up to perhaps one or two time steps before the approximated nucleation time. The mesh at the groove tip at that instant is checked to make sure that it is of good quality. If it is, then the rest of the computation proceeds without remeshing. If the mesh quality is bad, then the meshing parameters are readjusted and the calculations redone. However, if it is too difficult to obtain a good quality mesh at this particular time, then the calculations is set to end at one more time step earlier. This trial is then run, and the mesh is checked again. This procedure is used for every stress case. All in all, the objective is to create a good quality, sufficiently dense, mesh at the groove tip and then stop the remeshing. The rest of the calculations then move forward without remeshing until mesh failure.

The main goal here is to compare the nucleated crack size and nucleation time computed by the finite element procedure to those published by Yu and Suo (1999). Computations were done for $s = 1$, 4, 5, 6, 10, 15, and 20. For $s = 1$, Fig. 10 shows that the groove depth does indeed reach a constant level and no crack nucleation occurs. The steady state groove depth is found to be 5% different from that computed by Yu and Suo (1999). The two curves shown in Fig. 10 correspond to two different time steps. Fig. 11 presents the results for the cases where crack nucleation is expected. In all cases, the computed nucleation time is longer than those of Yu and Suo (1999) by less than a factor of two. Similarly, the final groove depths are similar to the ones obtained by Yu and Suo (1999) as shown in Fig. 12. Also, Fig. 12 shows that the numerical technique presented here yields the expected trend in the groove depth versus applied stress. Fig. 13 illustrates the convergence of the computed groove depth as a function of the time step size.

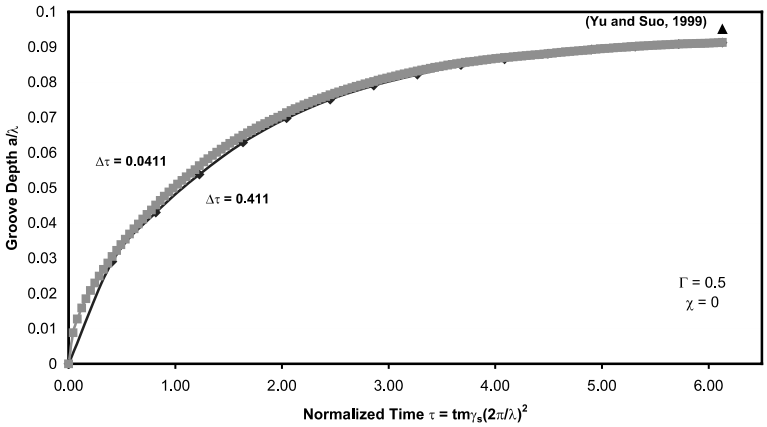

Fig. 10. Crack nucleation at a grain boundary: groove depth vs. normalized time for $s = 1$.

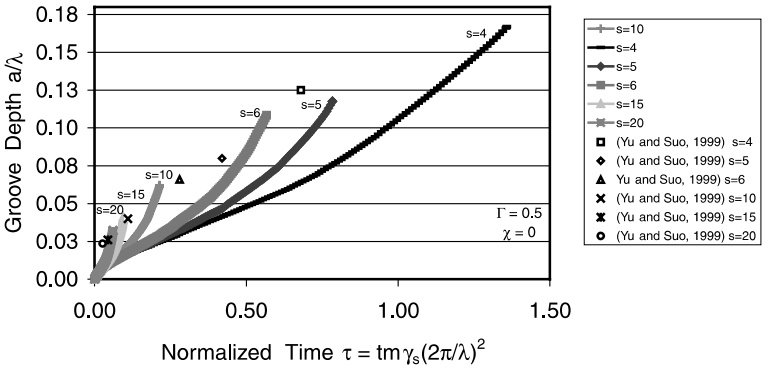

Fig. 11. Crack nucleation at a grain boundary: groove depth vs. normalized time.

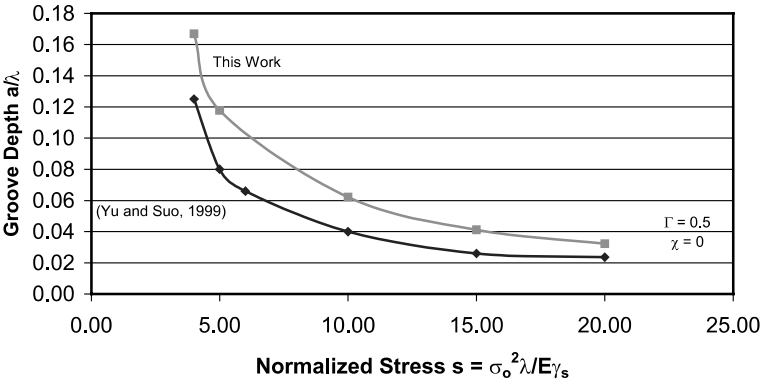

Fig. 12. Crack nucleation at a grain boundary: groove depth vs. normalized stress.

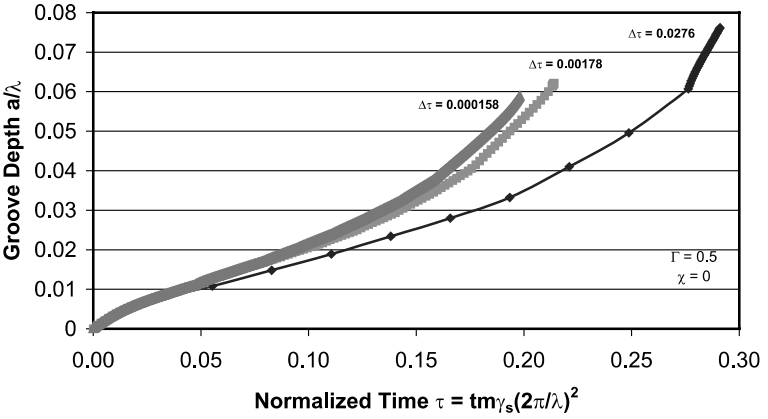

Fig. 13. Crack nucleation at a grain boundary: groove depth vs. normalized time for $s = 10$.

8. Concluding remarks

We have developed a general numerical technique, within the framework of the finite element method, to analyze and simulate the dissolution process. Both r- and h-adaptive refinements are used to conform the mesh to the evolving surface of the solid body, and to increase the mesh density by over three orders of magnitude in regions of high stress intensity and gradient. The flexibility and accuracy of the proposed method have been illustrated by solving a number of examples including a crack nucleation problem. Further work will concentrate on incorporating more realistic models (e.g., nonlinear kinetic laws, elastic–plastic solid models, etc.).

Acknowledgements

J.H.P. and T.J.B. have been supported by NSF through the grant CMS-9988788 (Dr. J. Larsen-Basse, program director). T.J.B. has also been supported by NASA Ames Research Center through the grant NAG 2-1327. J.L. and Z.S. have been supported by the National Science Foundation through the grant CMS-9820713. These supports are gratefully acknowledged.

References

Aziz, M.J., Sabin, P.C., Lu, G.-Q., 1991. The activation strain tensor: nonhydrostatic stress effects on crystal-growth kinetics. Phys. Rev. B 44, 9812–9816.

Baker, T.J., 1994. Triangulations, mesh generation and point placement strategies. in: Caughey, D.A., Hafez, M.M. (Eds.), Frontiers of Computational Fluid Dynamics, Wiley, New York.

Barlow, J., 1976. Optimal stress locations in finite element models. Int. J. Numer. Meth. Engng. 10, 243–251.

Barvosa-Carter, W., Aziz, M.J., 1998. Kinetically driven growth instability in stresses solids. Phys. Rev. Lett. 81, 1445–1448.

Bhate, D., Kumar, A., Bower, A.F., 2000. Diffuse interface model for electromigration and stress voiding. J. Appl. Phys. 87, 1712–1721.

Cash, J.R., Karp, A.H., 1990. ACM Trans. Math. Software 16, 201–222.

Chew, P., 1993. Guaranteed quality mesh generation for curved surfaces. Proc. Ninth Symp. Comp. Geom. ACM Press, pp. 274–280.

Chiu, C.H., Gao, H., 1993. Stress singularities along a cycloid rough surface. Int. J. Solids Struct. 30, 2981–3012.

Cocks, A.C.F., Gill, S.P.A., Pan, J., 1999. Modeling microstructure evolution in engineering materials. Adv. Appl. Mech. 36, 81–162.

Chuang, T., Fuller, E., 1992. Extended Charles-Hillig theory for stress corrosion cracking of glass. J. Am. Ceram. Soc. 75, 540–545.

Hillig, W.B., Charles, R.J., 1965. Surfaces, stress-dependent surface reactions, and strength. in: Zackay, V.F. (Ed.), High Strength Materials, Wiley, New York, pp. 682–705.

Hughes, T.J.R., 1987. The Finite Element Method, Prentice-Hall, Englewood Cliff, NJ.

Kim, K.-S., Hurtado, J.A., Tan, H., 1999. Evolution of a surface-roughness spectrum caused by stress in nanometer-scale chemical etching. Phys. Rev. Lett. 83, 3872–3875.

Lawson, C.L., 1977. Software for C^1 surface interpolation. in: Rice, J.R. (Ed.), Mathematical Software III, Academic Press, New York, pp. 161–194.

Lee, R.L., Gersho, P.M., Sani, R.L., 1979. Smoothing techniques for certain primitive variable solutions of the Navier stokes equation. Int. J. Numer. Meth. Engng. 14, 1785–1804.

Masud, A., Hughes, T.J.R., 1993. A space-time finite element method for fluid-structure interaction. Sudam Report No. 93-3, Stanford University, Stanford, CA.

Mullins, W., 1959. Flattening of a nearly plane solid surface due to capillarity. J. Appl. Phys. 30, 77–83.

Srolovitz, D.J., 1989. On the stability of surfaces of stressed solids. Acta Metall. 37, 621–625.

Sun, B., Suo, Z., Yang, W., 1997. A finite element method for simulating interface motion. I: Migration of phase and grain boundaries. Acta Mater. 45, 1907–1915.

Suo, Z., 1997. Motions of microscopic surfaces in materials. Adv. Appl. Mech. 33, 193–294.

Yang, W.H., Srolovitz, D.J., 1993. Cracklike surface instabilities in stressed solids. Phys. Rev. Lett. 71, 1593–1596.

Yu, H., Suo, Z., 1999. Delayed fracture of ceramics caused by stress-dependent surface reactions. Acta Mater. 47, 77–88.
Yu, H., Suo, Z., 2000. Stress-dependent surface reactions and implications for a stress measurement technique. J. Appl. Phys. 87, 1211–1218.
Zhang, Y.W., Bower, A.F., 1999. Numerical simulations of island formation in a coherent strained epitaxial thin film system. J. Mech. Phys. Solids 47, 2273–2297.
Zienkiewicz, O.C., Taylor, R.L., 1991. The Finite Element Method. McGraw-Hill, New York.